



Cite this: *RSC Adv.*, 2017, 7, 51538

Theoretical investigations on the structure–property relationships of Au₁₃ and Au_xM_{13–x} nanoclusters†

Ying Lv, Xi Kang,  Sha Yang, Tao Chen, Ao Liu, Haizhu Yu* and Manzhou Zhu *

As a fundamental building block in ultrasmall, noble metal nanoclusters, icosahedral Au_xM_{13–x} structures have recently attracted extensive research interest. In this study, density functional theory (DFT) and time-dependant DFT calculations have been carried out to investigate the structure–property (optical and electronic) relationships of a series of Au₁₃ and Au_xM_{13–x} (M = Au, Ag, Cu, and Pd) nanoclusters co-protected by phosphine and chloride ligands. It was found that the size of the peripheral ligands significantly affects the geometric structure: the larger exterior ligands (with a larger cone angle) result in relatively longer Au–M bond distances and weaker metallic interactions within the Au_xM_{13–x} core. Therefore, the optical peak (in the UV-vis spectrum) corresponding to the HOMO → LUMO transition red-shifts accordingly. When different foreign atom(s) are incorporated, the preferential doping site is different, and the electronic and optical structures alter accordingly.

Received 31st July 2017
Accepted 30th October 2017

DOI: 10.1039/c7ra08421h

rsc.li/rsc-advances

Introduction

In recent years, atomically precise ultrasmall gold nanoclusters (NCs) with diameters of <2 nm have attracted intensive research interest due to the promising applications in catalysis,¹ biomimetic materials^{2,3} and biotherapy.⁴ Thanks to the atomic precision, the icosahedral Au_xM_{13–x} building block has been frequently observed in different sized NCs. Depending on the chemical environment around the Au_xM_{13–x} structure, these NCs could be roughly categorized into three groups. First, in different Au_xM_{13–x} nanoclusters, the icosahedral Au_xM_{13–x} framework is protected directly by organic ligands (such as thiolate and phosphine). Second, the vertice- or face-sharing assembly of several Au_xM_{13–x} structures might be responsible for the metal framework of some relatively larger NCs, such as Au₂₅ (rod-like),^{5,6} Au₃₈,⁷ and Au₆₀.⁸ In the third group of NCs, the icosahedral Au_xM_{13–x} core is protected by the exterior metal–organic shell. Such a structure has been frequently observed in NCs such as Au₂₅ (spherical),⁹ Au₁₉ (ref. 10) and Au₂₀ NCs.¹¹ According to the recent studies, the structure and property of the metal core significantly affect the electronic, catalytic, and optical properties.¹² Therefore, the systematic investigation on the icosahedral Au_xM_{13–x} core will benefit the future exploration on the property of larger NCs.

Realizing the importance of the icosahedral core, chemists have extensively studied the structure–property relationships of the Au_xM_{13–x} NCs in recent years. For example, Kronik *et al.* successfully synthesized Au₁₃(PPh₃)₄(SC₁₂H₂₅)₄, and found that the co-protection of thiolates and phosphine ligands leads to the slight distortion of the icosahedral structure.¹³ Similarly, Wei and co-workers recently found that the framework of Au₁₃(PPh₃)₄(SC₁₂H₂₅)₄ is significantly disturbed by the solvent environment. They found that changing the solvent from ethanol to hexane induces the dissociation of the anionic SR ligands, and the rearrangement of the icosahedral core structure to a face-centred cubic (FCC) structure.¹⁴ Resultantly, the electronic structure remarkably changes from semiconducting to metallic state. Of note, the influence of the shell ligands on the geometric and electronic structures have also been reported elsewhere. For example, Konishi and co-workers successfully synthesized a series of Au₁₃ NCs co-protected by bidentate phosphine (Ph₂P–(CH₂)_m–PPh₂, *m* = 2–5) and chloride ligands. They found that the P : Cl ratio varies from 10 : 2 to 8 : 4 when *m* changes from 2 to 3–5, and the optical properties also change critically.^{15,16} After that, they further prepared another Au_xM_{13–x} NC, *i.e.* [Au₁₃(dppe)₅(C≡CPh)₂]³⁺ via the ligand exchange reaction of [Au₁₃(dppe)₅Cl₂]³⁺ (dppe is short for PPh₂CH₂CH₂PPh₂), and bore out the electronic coupling between the Au₁₃ core and the π-orbitals of acetylide.¹⁷ Aside from the mono-metallic Au₁₃ NCs, the alloy Au_xM_{13–x} NCs have also been successfully prepared in these years. For instance, Copley and Mingos synthesized three NCs, *i.e.* [Au₉M₄(PPh₂Me)₈Cl₄]⁺ (M = Au, Ag, Cu), and found that the optical properties of these three NCs are significantly different. The characteristic peaks in the UV-vis

Department of Chemistry, Center for Atomic Engineering of Advanced Materials, Anhui Province Key Laboratory of Chemistry for Inorganic/Organic Hybrid Functionalized Materials, Anhui University, Hefei, Anhui 230601, China. E-mail: yuhaizhu@ahu.edu.cn; zmz@ahu.edu.cn

† Electronic supplementary information (ESI) available. See DOI: 10.1039/c7ra08421h



spectrum blueshift with the incorporation of the Ag dopants, while were only slightly weakened when Cu atoms are doped.¹⁸

In addition to the experimental studies, theoretical methods have also been used to study the structure and properties of several Au₁₃ NCs. For example, Remacle and co-workers recently used density functional theory (DFT) calculations to study the modeling Au₁₃(SCH₃)₅(PH₃)₇ cluster, and found that the positions of the phosphines and thiolates significantly affect the geometric structure and electronic properties.¹⁹ In addition, comparing the UV-vis spectra of a series of Au₁₃, Au₂₅ and Au₂₈ NCs, they found that the increased charge density of the metal core (Au₁₃ for Au₁₃, Au₁₃ for Au₂₅ and Au₂₀ for Au₂₈) is responsible for the red-shift of the optical absorption bands.

Despite the aforementioned studies, the systematic understanding on the effect of different ligands (including both the number and the structure of the protecting ligands), and especially the doping effect in the alloy Au_xM_{13-x} NCs, are rarely reported. In this study, we carried out theoretical investigation on a series of icosahedral Au₁₃ and alloy Au_xM_{13-x} NCs with DFT and TD-DFT calculations to elucidate the structure–property relationships. The monometallic Au₁₃ NCs including [Au₁₃-(PR₃)₈Cl₄]⁺ and [Au₁₃(PR₃)₁₀Cl₂]³⁺ (R = Me, Ph) were chosen to examine ligand effect of the phosphine and chloride ligands.²⁰ Meanwhile, the doping effect was explored by comparing the structure and property of the monometallic [Au₁₃(PR₃)₈Cl₄]⁺ NCs with the alloy counterparts including [Au₉Ag₄(PPh₂Me)₈Cl₄]⁺, [Au₉Cu₄(PPh₂Me)₈Cl₄]⁺, and [Au₁₂Pd(PPh₃)₈Cl₄], whose structures have been precisely elucidated by single X-ray crystallography.^{18,20,21} This study can provide deep understanding on the structure–property relationships in the icosahedral metal NCs, and will also benefit the future explorations on larger NCs assembled with Au_xM_{13-x}.

Computational details

The geometry optimization of all NCs was carried out with the ADF software,²² using GGA: PBE/TZP method.²³ The time-dependent LB94/TZP method and the scalar relativistic were used for UV-vis spectra calculation, and the lowest 150 singlet excited states were calculated.²⁴ The Kohn–Sham (KS) orbital analyses were performed with Gaussian 09 suite of program,²⁵ using the long-range corrected functional CAM-B3LYP functional.²⁶ The LanL2DZ basis set and the effective core potential were used for the metal atoms (*i.e.* Au, Ag, Cu, Pd), and the total electron basis set 6-31G(d) was used for all other atoms.

We first compared the calculated Au–M bond distances with the experimental ones obtained from the single crystal X-ray crystallography to examine the reliability of theoretical calculations.^{18,20,21} As shown in Fig. 1, despite the Au–M bond distances are slightly overestimated by theoretical methods, the overall correlation between the calculated and experimental bond distances are acceptable: the linear coefficient (*R*) is 0.9045 for the 84 data, and the square deviation (SD) is 0.0467 Å (Fig. 1). The good correlation of the experimental and calculated Au–M (M = Au, Ag, Cu) bond distances verifies the theoretical methods.

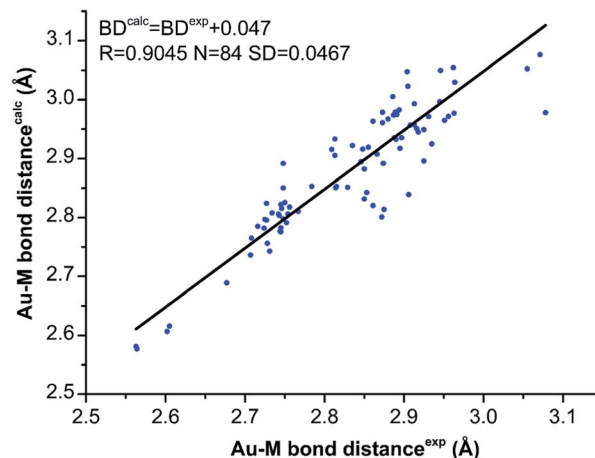


Fig. 1 The correlation of the experimental (from single-crystal X-ray crystallography) and the calculated Au–M (M = Au, Ag, Cu) bond distances for [Au₉Ag₄(PPh₂Me)₈Cl₄]⁺ and [Au₉Cu₄(PPh₂Me)₈Cl₄]⁺.

Results and discussions

The ligand effect in Au₁₃ NCs co-protected by phosphine and chloride ligands

In the past decades, a series of Au₁₃ NCs co-protected by phosphine and chloride ligands have been synthesized. For example, Mingos and co-workers used the *in situ* reduction of Au(PR₃)Cl (with Ti(η-C₆H₅Me)) to prepare the Au NC, and determined the atomic structure to be [Au₁₃(PMe₂Ph)₁₀Cl₂]³⁺ with the single crystal X-ray analysis.²⁰ After that, they also prepared [Au₁₃(PMePh₂)₈Cl₄]⁺ via the reaction of [Au₁₁-(PMePh₂)₁₀]³⁺ with AuCl(PMePh₂) in CH₂Cl₂.¹⁸ Recently, Konishi and co-workers prepared the [Au₁₃(POct₃)₈Cl₄]⁺ (Oct = octyl) by reducing Au(POct₃)Cl with NaBH₄ in aqueous THF.¹⁵

In accordance with the aforementioned studies, the structures, UV-vis spectra and KS-orbitals of the four Au₁₃ NCs co-protected by chloride and phosphine ligands, *i.e.*

Table 1 The average bond length (the data in parentheses are experimental values) and the average Hirshfeld charge on selected atoms in NC0–3 (Å)

Bond distance	NC0	NC1	NC2	NC3
Au ^{center} –Au ^{shella}	2.813	3.012 (2.769)	2.822	2.845
Au ^{center} –Au ^{Cl}	2.815	2.993 (2.715)	2.807	2.776
Au ^{center} –Au ^P	2.811	3.016 (2.780)	2.830	2.880
Au ^{Cl} –Cl	2.372	2.362 (2.297)	2.394	2.406
Au ^P –P	2.310	2.342 (2.286)	2.335	2.372
Cone angle (PR ₃)	46.7°	60.9°	74.7°	76.4°
Hirshfeld charge				
Au ^{center}	−0.005	−0.021	0.000	0.000
Au ^{shell}	0.014	0.047	0.037	0.046
Au ^P	0.015	0.044	0.038	0.046
Au ^{Cl}	0.012	0.061	0.035	0.053
Cl	−0.337	−0.326	−0.281	−0.230

^a Note: Au^{shell} include both the Au^{Cl} and Au^P atoms, while Au^{Cl} and Au^P denote the Au atoms connecting with Cl and P atoms, respectively.



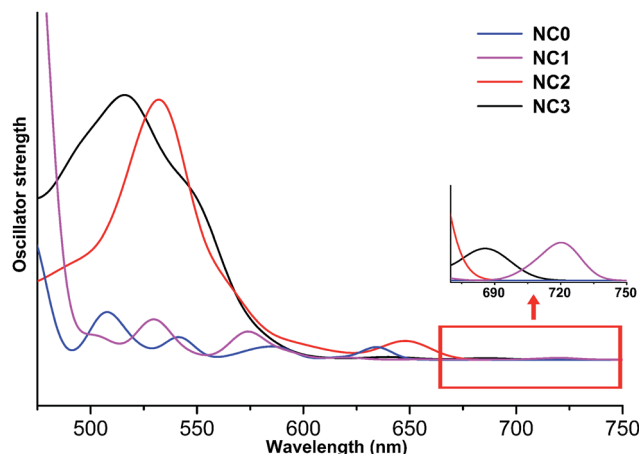


Fig. 2 Theoretical UV-vis spectra of NC0, NC1, NC2 and NC3.

$[\text{Au}_{13}(\text{PMe}_3)_8\text{Cl}_4]^+$, $[\text{Au}_{13}(\text{PPhMe}_2)_{10}\text{Cl}_2]^{3+}$, $[\text{Au}_{13}(\text{PPh}_2\text{Me})_8\text{Cl}_4]^+$, and $[\text{Au}_{13}(\text{PPh}_3)_8\text{Cl}_4]^+$ were calculated. Note that $[\text{Au}_{13}(\text{PMe}_3)_8\text{Cl}_4]^+$ was used to model the experimentally characterized $[\text{Au}_{13}(\text{POct}_3)_8\text{Cl}_4]^+$, so as to reduce the computational cost. For clarity, these four NCs are designated as NC0, NC1, NC2, and NC3, respectively. The 0–3 here denote the number of phenyl groups on the PR_3 ligand in each NC.

Comparing the selected structural parameters of the optimized geometries (Table 1), we found that the average Au–P and Au–Cl distances are comparable in different NCs. By contrast, the Au–Au bond distances change remarkably. The average $\text{Au}^{\text{center}}\text{--Au}^{\text{shell}}$ bond distance in NC1 is significantly longer than those in NC0/NC2/NC3. The phenomenon is mainly caused by the stronger steric repulsion between the 10 phosphine ligands in NC1 (compared to that between the 8 phosphine ligands in all other NCs). For the same reason, the average $\text{Au}^{\text{center}}\text{--Au}^{\text{P}}$ bond distance in NC1 is also relatively longer than those in NC0/NC2/NC3 (Table 1).

To comprehend why $[\text{Au}_{13}(\text{PMe}_2\text{Ph})_{10}\text{Cl}_2]^{3+}$ (NC1) is preferentially formed over $[\text{Au}_{13}(\text{PMe}_2\text{Ph})_8\text{Cl}_4]^+$ (analogue of NC0/NC2/NC3), we analysed the cone angle of the phosphine ligands in all these Au_{13} NCs. According to the previous studies, the cone angle of the surface ligands directly correlates with the composition and size of the nanoclusters.^{27,28} As shown in Table 1, the cone angle of PMe_2Ph in NC1 is significantly smaller than the those of PPh_2Me in NC2 and PPh_3 in NC3. The smaller cone angle of PMe_2Ph enables the incorporation of more phosphine ligands in NC1. Herein, it is noteworthy that the theoretical modelling of POct_3 with PMe_3 in NC0 significantly underestimate the cone angle. The small cone angle of PMe_3 might strongly disfavours the small cluster sizes, and this is also the reason why only large sized NCs (with metal atoms >32)^{29,30} have been reported when PMe_3 are dominant ligands. We suppose that the relatively larger cone angle of the PPh_3 ligand also explains why PPh_3 is observed as a successful ligand for $[\text{Au}_{11}(\text{PPh}_3)_x\text{Cl}_y]^q$ synthesis,³¹ but not yet for $[\text{Au}_{13}(\text{PPh}_3)_x\text{Cl}_y]^q$.

According to the aforementioned discussions, the cone angle of the phosphine ligands determines the ratio of the phosphine and chloride ligands, as well as the Au–Au bond distances in the

Au_{13} core. This conclusion is also supported by the Hirshfeld charge analysis (Table 1). The charge on the Au^{shell} atoms of NC1 is slightly more positive than those of the other NCs, predominantly due to the weakened σ -donating ability of the phosphine ligand therein. Meanwhile, the center Au atom in these NCs is all nearly charge neutral (Table 1).

Regarding the optical properties, the absorption peaks are systematically overestimated by 100 nm due to the deficiency of DFT methods in treating the excited states. The similar observation was also reported in previous studies.³² Nevertheless, comparing the curves of different NCs (Fig. 2), we found that the UV-vis absorption spectra of NC1, NC2, NC3 are similar, while the peak splitting was observed in the spectrum of NC0. Similar separation of the optical bands induced by methyl groups has also been reported in Sun's recent study.³³ As shown in Fig. 2, the first band of NC1, NC2 and NC3 appear at ~ 720 nm, 650 nm and 685 nm, respectively. All these bands correspond to the $\text{HOMO} \rightarrow \text{LUMO}$ transition, and the weakness of the peaks implies that the transition is optically forbidden. In addition to the $\text{HOMO} \rightarrow \text{LUMO}$ transition, the prominent absorption peak of NC2 at 540 nm mainly arises from the transition from the 3-fold quasi-degenerate HOMO manifold to the LUMO+9, LUMO+10 and LUMO+11 set. For NC3, the prominent peak at 520 nm is mainly caused by the transition from the doubly degenerate HOMO and HOMO–1 set to the LUMO+4, LUMO+5 and LUMO+6 set. For NC0, the $\text{HOMO} \rightarrow \text{LUMO}$ transition appears at ~ 640 nm, and the prominent peak (~ 580 nm) corresponds to HOMO–1, HOMO–2 \rightarrow LUMO+3, +4, +5 (Fig. 2).

Fig. 3 shows the KS-orbital analysis of all these NCs. The discrete energy levels of NC0 correlates with its separate and weak optical bands (Fig. 2 & 3a). By contrast, the introduction of phenyl substituent in the phosphine ligands results in the degeneracy of the energy levels (Fig. 3b–d). The degenerate orbitals explain the peak broadening in the UV-vis spectra of NC1, NC2 and NC3.

Aside from the energy levels, the atomic contributions of the frontier orbitals of all these Au_{13} NCs are similar. As shown in Fig. 3, $\text{Au}(6\text{s})$ and $\text{Au}(5\text{d})$ are mainly responsible for all the HOMOs (highest occupied molecular orbitals) and LUMOs (lowest unoccupied molecular orbitals). Therefore, the active electrons mainly locate in the Au_{13} core. In addition, the $\text{Au}(6\text{s})$ orbitals make major contribution to the higher HOMOs and LUMOs, while the $\text{Au}(5\text{d})$ orbitals contribute predominantly to the lower HOMOs (Fig. 3a, c and d). To this end, the first band of all the Au_{13} NCs correspond to interband transition of $\text{d} \rightarrow \text{sp}$. This conclusion is consistent with the recent theoretical studies on the electronic and optical analysis of the small sized NCs (such as Au_{18} NC).³⁴

Combining the key structural parameters and the optical & electronic properties of different Au_{13} NCs, we found that the cone angle of the PR_3 ligands dominates the composition and structure of the Au_{13} NCs. The larger PR_3 ligand encourages the structure of $[\text{Au}_{13}(\text{PR}_3)_8\text{Cl}_4]^+$, while the PR_3 with small cone angle facilitates the formation of $[\text{Au}_{13}(\text{PR}_3)_{10}\text{Cl}_2]^{3+}$. The average $\text{Au}^{\text{center}}\text{--Au}^{\text{shell}}$ bond distance of $[\text{Au}_{13}(\text{PR}_3)_{10}\text{Cl}_2]^{3+}$ is relatively longer than that of $[\text{Au}_{13}(\text{PR}_3)_8\text{Cl}_4]^+$, and the weakened bonding



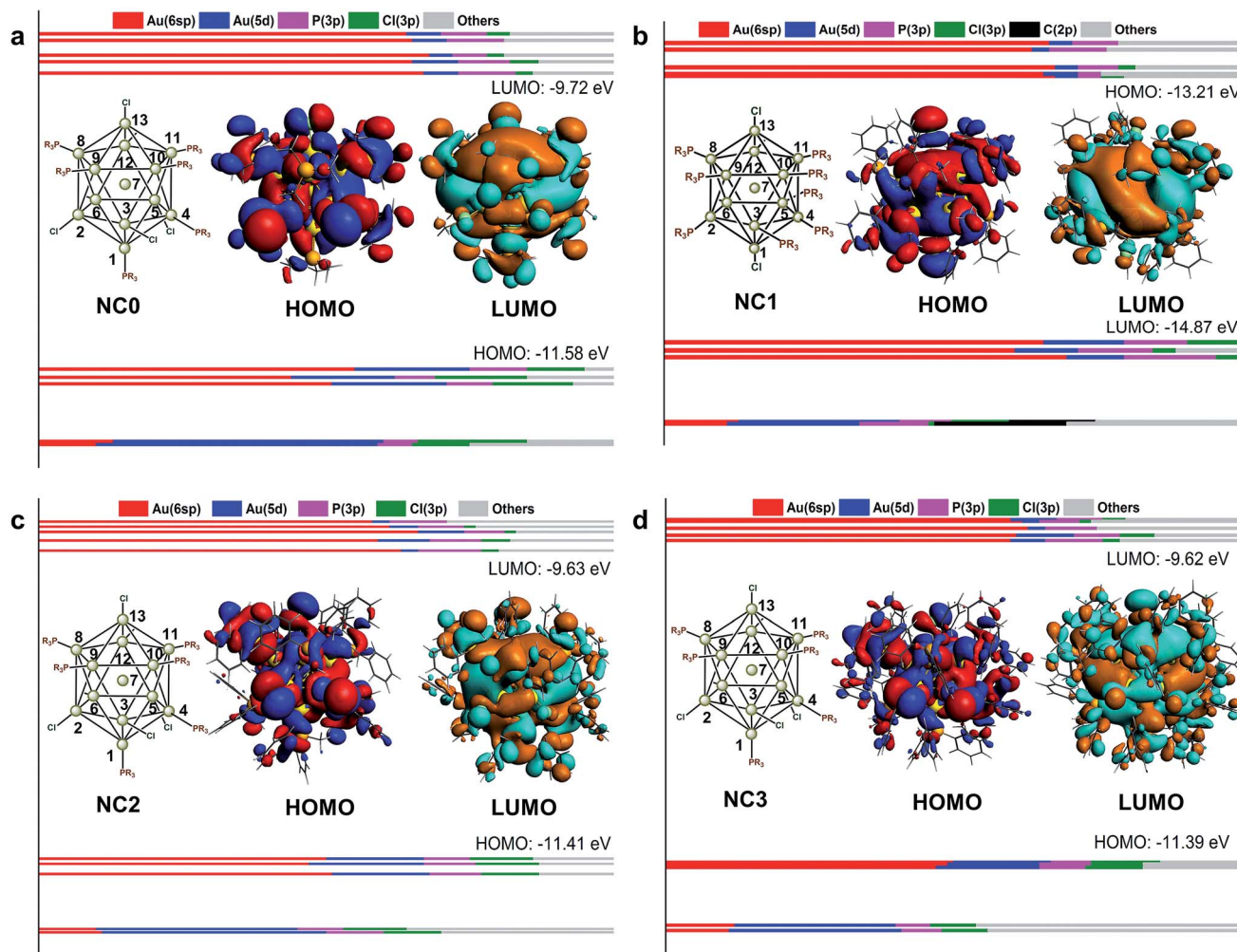


Fig. 3 The HOMO, LUMO plots and KS orbitals of NC0 (a), NC1 (b), NC2 (c) and NC3 (d).

strength in the former case further results in the lower HOMO \rightarrow LUMO transition.

For in-depth understanding on the orbital distributions of Au_{13} NCs, we referred to the superatom models.³⁵ According to this model, all these Au_{13} NCs are 8-electron clusters with 1S^2 , 1P^6 jellium orbitals (S, P and D orbitals in superatom correspond to the atomic s, p and d orbitals, respectively). The HOMOs of all these Au_{13} NCs feature the characteristic of P orbital,^{36,37} while the LUMOs of all these Au_{13} NCs feature the D orbital characteristics (Fig. 3).³⁷

The doping effect of the foreign (Ag, Cu, and Pd) atom(s)

According to the recent experimental studies, different foreign metal (Ag, Cu, and Pd) atom(s) with the electronic structures similar to Au could be doped into the Au_{13} NCs.^{18,21} Interestingly, these metals were preferentially doped into different sites. For example, Mingos and co-workers synthesized the shell doped $[\text{Au}_9\text{M}_4(\text{PMePh}_2)_8\text{Cl}_4]^+$ ($\text{M} = \text{Cu}, \text{Ag}$) NCs *via* the reaction of $[\text{Au}_{11}(\text{PMePh}_2)_{10}]^{3+}$ with $\text{MCl}(\text{PMePh}_2)$.¹⁸ Recently, the core doped $[\text{PdAu}_{12}(\text{PPh}_3)_8\text{Cl}_4]$ has been synthesized by photolysis of $(\text{Ph}_3\text{P})_2\text{Pd}(\text{N}_3)_2$, Ph_3PAuN_3 and Ph_3PAuCl in THF solvent.²¹ To

understand the doping preference for different metal atoms, we first examined the relative energy of the $\text{Au}_x\text{M}_{13-x}$ structures with the foreign atom doping at different site. The 13 possible doping sites on Au_{13} were roughly categorized into six groups: the metal center atom, the shell atom coordinating with the phosphine ligand (adjacent to three Au–Cl bonds for *shell-a* and adjacent to two Au–Cl bonds for *shell-b/c*), and the shell atom connecting with chloride (adjacent to one Au–Cl bond for *shell-d*, and adjacent to none Au–Cl bond for *shell-e*). The details are given in Fig. 4b, and the typical positions of 7, 9, 6, 11, 3, and 13 are used for the following discussion. For clarity reasons, the core-doped alloy NCs were taken as the reference, and the energy difference between the other structures and the core-doped one is used to evaluate their relatively stability. From Table 2, it can be seen that the relative energies of the *shell-a/b/c* doped products are comparable for each type of alloy system (note: these positions correspond to the different shell Au^{P} sites, see Fig. 4b). Similarly, the relative energies of the *shell-d* and *shell-e* doped products are also alike (note: both positions correspond to the Au^{Cl} sites). The results imply that the differences in the adjacent atomic environment (such as the *shell-a/b/*



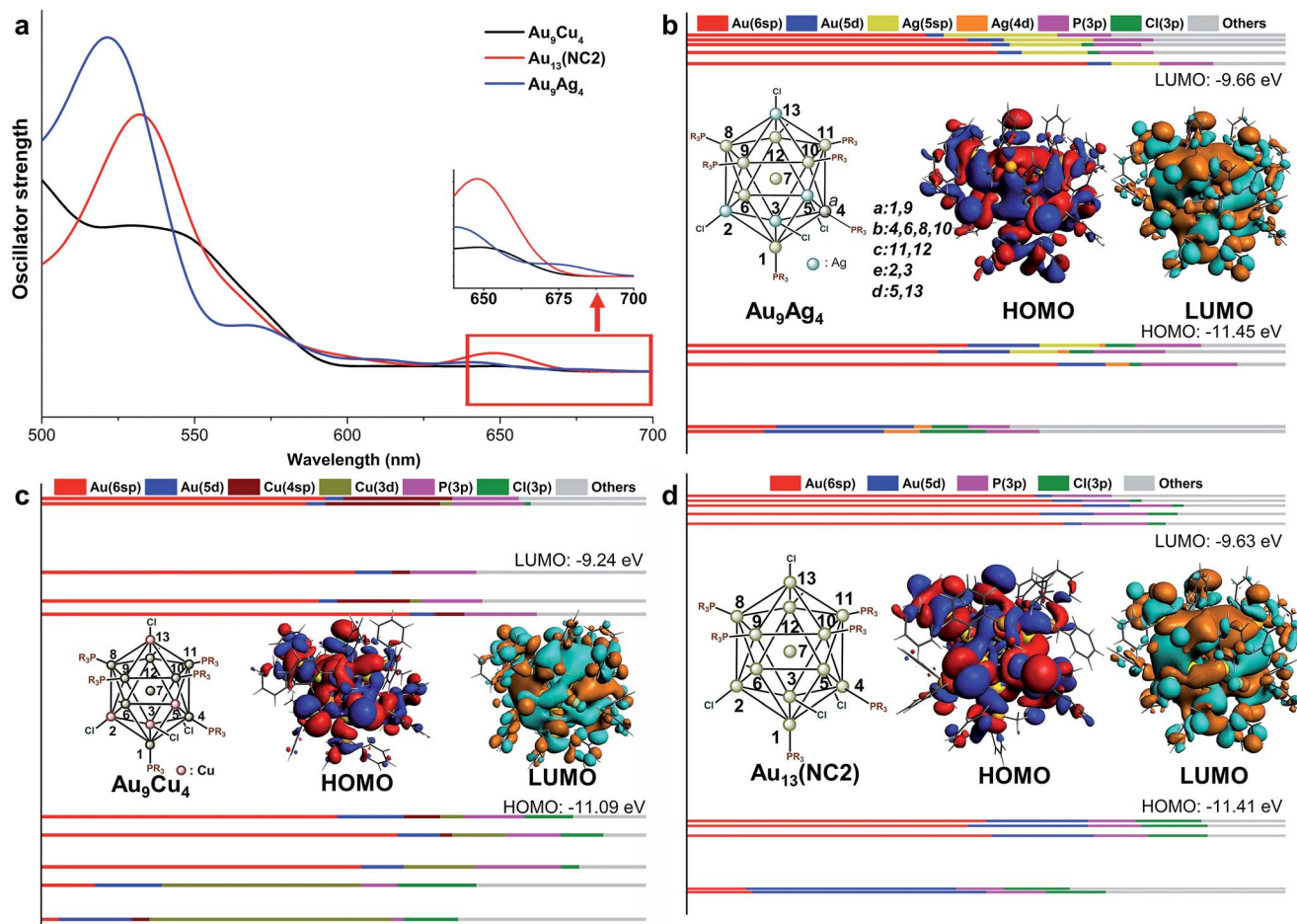


Fig. 4 The UV-vis spectra of Au_9Cu_4 , Au_{13} and Au_9Ag_4 (a); the component of KS orbitals of Au_{13} (b), Au_9Cu_4 (c) and Au_9Ag_4 (d).

Table 2 Comparison on the site preference of different doping sites for Ag, Cu, and Pd (in eV)

	$\Delta E(\text{Au}_{12}\text{M}^{\text{shell}} - \text{Au}_{12}\text{M}^{\text{center}})$		
	M = Ag	M = Cu	M = Pd
Shell-a	-0.56	-0.18	0.97
Shell-b	-0.51	-0.12	0.87
Shell-c	-0.45	-0.09	0.90
Shell-d	-0.83	-0.51	1.02
Shell-e	-0.86	-0.58	1.06

c positions of Au^{P}) hardly affect the doping facility. However, for each doping system (with specific foreign atom), the relative energy of the $\text{Au}^{\text{center}}$ doped one is distinct from that of the Au^{P} or Au^{Cl} doped structure. Therefore, the doping easiness is mainly determined by the chemical environment ($\text{Au}^{\text{center}}$ or Au^{P} or Au^{Cl}).

According to Table 2, Ag and Cu atoms preferentially locate on the shell sites, and especially the Au^{Cl} positions (shell-d/e). By contrast, the doping of Pd occurs preferentially on the core site, while all the shell-doping modes are thermodynamically disfavoured. The theoretical results are in good agreement with the

experimental characterization.²¹ The distinct doping preference of Ag, Cu and Pd is mainly determined by the Au–M interactions. The intermetallic interaction of Au with different metal atoms follows the order of $\text{Cu} < \text{Ag} < \text{Au} < \text{Pd}$,^{38,39} and thus the Ag and Cu atom(s) tend to be doped in the shell while Pd tends to be doped in the center.

The geometric and electronic structure of the surface doped $[(\text{Au}_x\text{M}_{13-x})\text{P}_8\text{Cl}_4]^+$

In our study, the aforementioned four $\text{Au}_x\text{M}_{13-x}$ NCs were selected for discussions on the doping effect of the foreign atoms, and they are labelled as Au_9M_4 ($\text{M} = \text{Cu}, \text{Ag}$), Au_{13} (i.e. NC2) and Au_{12}Pd , respectively. Comparing the key structural

Table 3 The selected average bond length of Au_9Cu_4 , Au_{13} and Au_9Ag_4 (the data in parenthesis are experimental value)

Bond distance	Au_9Ag_4	Au_{13}	Au_9Cu_4
$\text{Au}^{\text{center}} - \text{M}^{\text{shell}}$	2.821(2.773)	2.822	2.728(2.686)
$\text{M}^{\text{Cl}} - \text{Cl}$	2.414(2.378)	2.395	2.164(2.134)
$\text{Au}^{\text{center}} - \text{M}^{\text{Cl}}$	2.849(2.828)	2.807	2.595(2.584)



Table 4 The average bond length (the data in parenthesis are experimental value) and the average Hirshfeld charge on selected atoms in Au_{12}Pd and NC3 (Å)

Bond distance	Au_{12}Pd	NC3
$\text{M}^{\text{center}}-\text{Au}^{\text{shell}}$	2.880(2.745)	2.845
$\text{M}^{\text{center}}-\text{Au}^{\text{Cl}}$	2.801(2.728)	2.776
$\text{M}^{\text{center}}-\text{Au}^{\text{P}}$	2.920(2.754)	2.880
$\text{Au}^{\text{Cl}}-\text{Cl}$	2.438(2.385)	2.406
$\text{Au}^{\text{P}}-\text{P}$	2.356(2.299)	2.372
Hirshfeld charge		
M^{center}	0.121	0.002
Au^{shell}	0.020	0.050
Au^{P}	0.023	0.046
Au^{Cl}	0.018	0.053
Cl	-0.265	-0.230

parameters in the Au_9M_4 NCs (Table 3), we found that the average $\text{Au}^{\text{center}}-\text{M}^{\text{shell}}$ distances in Au_{13} and Au_9Ag_4 NCs are very close, while the related bond distance in Au_9Cu_4 is relatively shorter. This phenomenon is mainly attributed to the smaller atomic radii of Cu compared with those of Au and Ag atoms (Cu: 1.28 Å, Au/Ag: 1.44 Å). For this reason, the average $\text{Au}^{\text{center}}-\text{Cu}^{\text{Cl}}$ bond distances in Au_9Cu_4 is significantly shorter than that of the $\text{Au}^{\text{center}}-\text{Ag}^{\text{Cl}}$ in Au_9Ag_4 and $\text{Au}^{\text{center}}-\text{Au}^{\text{Cl}}$ in Au_{13} (Table 3).

The theoretical UV-vis spectra of Au_9M_4 (M = Cu, Ag) and Au_{13} were given in Fig. 4a. Compared with the lowest-energy optical band of Au_{13} (~650 nm), the HOMO → LUMO transition of Au_9Ag_4 red shifts to 675 nm. In contrast, the HOMO → LUMO transition of Au_9Cu_4 is retained at 650 nm. Therefore, the Cu dopants make little perturbation to the energy of the lowest-energy optical band.

According to the KS-orbital analysis (Fig. 4b–d), the highest occupied orbitals are predominantly constituted by Au(6sp) orbitals, which also make the major contributions to the LUMOs. Therefore, the HOMO → LUMO transitions in all these NCs correspond to the sp → sp transitions. In addition, in the

UV-vis spectra of Au_9Cu_4 , the prominent shoulder peak at ~550 nm is mainly induced by the mixed transition of HOMO, HOMO–1 to the LUMO+6, +7, +8, +9 set (component mainly composed by ligands). The atomic contribution for such transitions is in accordance with the metal to ligand charge transfer (MLCT). With respect to the superatom model, the HOMOs of all these NCs show the P feature, while the HOMO of Au_9Ag_4 is slightly different (Fig. 4b) due to the electron density overlap between the two adjacent Ag atoms. Meanwhile, the LUMO of each NC figures the D orbital characteristic.

The geometric and electronic structure of the core doped Au_{12}Pd NC

Comparing the optimized geometries of Au_{12}Pd and its mono-metallic counterpart NC3, the average $\text{Au}^{\text{center}}-\text{Au}^{\text{shell}}$ bond length in NC3 is shorter than the average $\text{Pd}^{\text{center}}-\text{Au}^{\text{shell}}$ bond distance in Au_{12}Pd . In addition, both the average $\text{M}^{\text{center}}-\text{Au}^{\text{P}}$ and $\text{M}^{\text{center}}-\text{Au}^{\text{Cl}}$ bond length in Au_{12}Pd are relatively longer than the related ones in NC3 (Table 4). Similar to the aforementioned discussions, the relatively longer Au–Pd distances result in weakened intermetallic interactions and the significant red shift of the first band (685 nm for NC3 to 835 nm for Au_{12}Pd in Fig. 2 and 5a). For Au_{12}Pd , the peak at 740 nm and the shoulder peak at 640 nm mainly arise from the transition of HOMO–1, 2 → LUMO+3, 4 and HOMO–1, 2 → LUMO+7, 8, respectively. From KS-orbital in Fig. 5, the HOMO of Au_{12}Pd is mainly composed by Pd(4p), Au(6sp) and Au(5d) orbitals, while the Pd(4p) and Au(5d) atomic orbitals make almost no contribution to the LUMOs (Fig. 5b). Therefore, the mismatched orbital character of HOMO and LUMO results in the weakness of the first band.

Examining the charge distribution of Au_{12}Pd , it can be seen that the electron density on the core Pd atom is significantly more positive than the core Au atom in NC3 (Table 4). Meanwhile, the electron density on the shell Au atoms are all increased in Au_{12}Pd . Therefore, the results unambiguously show the charge transfer from Pd to Au. This conclusion is similar to the XPS characterization on the recently reported Au_{24}Pd alloys.⁴⁰

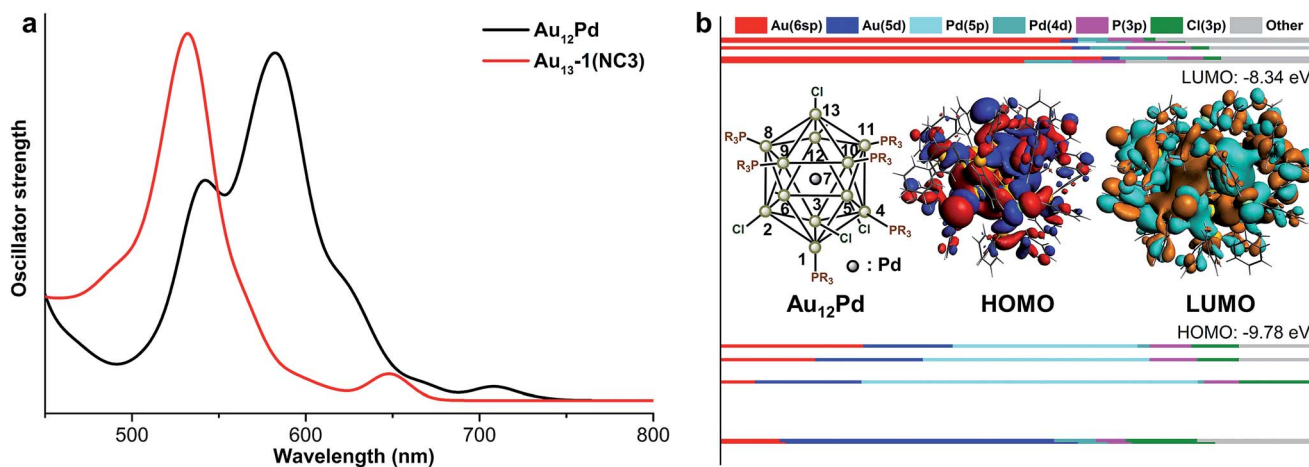


Fig. 5 The UV-vis spectra of Au_{12}Pd and Au_{13-1} (a), the component of KS orbitals of Au_{12}Pd (b).



Conclusions

In this study, DFT and TD-DFT calculations were carried out to obtain the geometric and electronic structures of a series of Au_{13} and $\text{Au}_x\text{M}_{13-x}$ ($\text{M} = \text{Au}, \text{Ag}, \text{Cu}, \text{Pd}$) NCs. It was found that PR_3 ligands play the prominent role in the geometric structure in Au_{13} NCs due to the steric bulkiness. The bulkier PR_3 with relatively larger cone angle favours the structure of $[\text{Au}_{13}(\text{PR}_3)_8\text{Cl}_4]^+$ (and even smaller-sized NCs such as M_{11}), while the PR_3 with smaller cone angle encourages the formation of $[\text{Au}_{13}(\text{PR}_3)_{10}\text{Cl}_2]^{3+}$ (or larger-sized NCs). The incorporation of more phosphine ligands results in the weaker Au–P and Au–Au interactions, associated with lowered HOMO–LUMO gap and the red shift of the related peak on UV-vis spectra. In addition, when different foreign atoms are doped into the Au_{13} NCs, preferential sites might be totally different. Ag and Cu atoms prefer the shell sites of the $\text{Au}_x\text{M}_{13-x}$ core, and especially in the sites connecting with Cl atom. By contrast, Pd prefers the central site of the icosahedral core. The doping preference significantly affects the geometric structure and the frontier orbitals. The Pd dopant leads to relatively longer Au–M distances within the icosahedral core, while the Au–M bond distances are significantly shorter when Cu atoms are incorporated. The relative energy of the HOMO \rightarrow LUMO transition of different $\text{Au}_x\text{M}_{13-x}$ NCs follows the order of $\text{Au}_{12}\text{Pd} < \text{Au}_9\text{Ag}_4 < \text{Au}_{13} \sim \text{Au}_9\text{Cu}_4$. The present study provides deep understanding on the ligand and doping effect in the icosahedral NCs, and will hopefully benefit the future investigation on structure–property correlations of larger NCs.

Conflicts of interest

The authors declare no competing financial interest.

Acknowledgements

We acknowledge financial support from NSFC (21672001, 21372006, 21631001 & U1532141), the Ministry of Education, the Education Department of Anhui Province, 211 Project of Anhui University. We thank the National Supercomputing Centre in Shenzhen for providing the computational resources and Gaussian 09 software.

Notes and references

- G. Li, H. Abroshan, Y. Chen, R. Jin and H. J. Kim, *J. Am. Chem. Soc.*, 2015, **137**, 14295.
- J. Sun and Y. Jin, *J. Mater. Chem. C*, 2014, **2**, 8000.
- D. An, J. Su, J. K. Weber, X. Gao, R. Zhou and J. Li, *J. Am. Chem. Soc.*, 2015, **137**, 8412.
- B. Khlebtsov, E. Tuchina, V. Tuchin and N. Khlebtsov, *RSC Adv.*, 2015, **5**, 61639.
- Y. Song, S. Jin, X. Kang, J. Xiang, H. Deng, H. Yu and M. Zhu, *Chem. Mater.*, 2016, **28**, 2609.
- J. Nishigaki, S. Yamazoe, S. Kohara, A. Fujiwara, W. Kurashige, Y. Negishid and T. Tsukuda, *Chem. Commun.*, 2014, **50**, 839.
- O. Lopez-Acevedo, H. Tsunoyama, T. Tsukuda, H. Häkkinen and C. M. Aikens, *J. Am. Chem. Soc.*, 2010, **132**, 8210.
- Y. Song, F. Fu, J. Zhang, J. Chai, X. Kang, P. Li, S. Li, H. Zhou and M. Zhu, *Angew. Chem., Int. Ed.*, 2015, **54**, 8430.
- T. W. Ni, M. A. Tofanelli, B. D. Phillips and C. J. Ackerson, *Inorg. Chem.*, 2014, **53**, 6500.
- X.-K. Wan, Q. Tang, S.-F. Yuan, D.-e. Jiang and Q.-M. Wang, *J. Am. Chem. Soc.*, 2015, **137**, 652.
- X.-K. Wan, S.-F. Yuan, Z.-W. Lin and Q.-M. Wang, *Angew. Chem., Int. Ed.*, 2014, **53**, 2923.
- (a) Z. Wu and R. Jin, *Nano Lett.*, 2010, **10**, 2568; (b) R. Ouyang and D.-e. Jiang, *ACS Catal.*, 2015, **5**, 6624; (c) E. Pohjolainen, H. Häkkinen and A. Clayborne, *J. Phys. Chem. C*, 2015, **119**, 9587.
- O. Guliamov, A. I. Frenkel, L. D. Menard, R. G. Nuzzo and L. Kronik, *J. Am. Chem. Soc.*, 2007, **129**, 10978.
- Y. Li, H. Cheng, T. Yao, Z. Sun, W. Yan, Y. Jiang, Y. Xie, Y. Sun, Y. Huang, S. Liu, J. Zhang, Y. Xie, T. Hu, L. Yang, Z. Wu and S. Wei, *J. Am. Chem. Soc.*, 2012, **134**, 17997.
- Y. Shichibu, K. Suzuki and K. Konishi, *Nanoscale*, 2012, **4**, 4125.
- Y. Shichibu and K. Konishi, *Small*, 2010, **6**, 1216.
- M. Sugiuchi, Y. Shichibu, T. Nakanishi, Y. Hasegawa and K. Konish, *Chem. Commun.*, 2015, **51**, 13519.
- R. C. B. Copley and D. M. Mingos, *J. Chem. Soc., Dalton Trans.*, 1996, 491.
- G. Lugo, V. Schwanen, B. Fresch and F. Remacle, *J. Phys. Chem. C*, 2015, **119**, 10969.
- C. Briant, B. C. Theobald, J. White, L. Bell and D. M. Mingos, *J. Chem. Soc., Chem. Commun.*, 1981, 201.
- M. Laupp and J. Strähle, *Z. Naturforsch., A: Phys. Sci.*, 1995, **50**, 1369.
- G. T. Velde, F. M. Bickelhaupt, E. J. Baerends, C. F. Guerra, S. J. A. V. Gisbergen, J. G. Snijders and T. Ziegler, *J. Comput. Chem.*, 2001, **22**, 931.
- (a) J. P. Perdew, K. Burke and M. Ernzerhof, *Phys. Rev. Lett.*, 1996, **77**, 3865; (b) M. Ernzerhof and G. E. Scuseria, *J. Chem. Phys.*, 1999, **110**, 5029.
- R. van Leeuwen and E. J. Baerends, *Phys. Rev. A: At., Mol., Opt. Phys.*, 1994, **49**, 2421.
- M. J. Frisch, G. W. Trucks, H. B. Schlegel, G. E. Scuseria, M. A. Robb, J. R. Cheeseman, G. Scalmani, V. Barone, B. Mennucci, G. A. Petersson, H. Nakatsuji, M. Caricato, X. Li, H. P. Hratchian, A. F. Izmaylov, J. Bloino, G. Zheng, J. L. Sonnenberg, M. Hada, M. Ehara, K. Toyota, R. Fukuda, J. Hasegawa, M. Ishida, T. Nakajima, Y. Honda, O. Kitao, H. Nakai, T. Vreven, J. A. Montgomery Jr, J. E. Peralta, F. Ogliaro, M. Bearpark, J. J. Heyd, E. Brothers, K. N. Kudin, V. N. Staroverov, T. Keith, R. Kobayashi, J. Normand, K. Raghavachari, A. Rendell, J. C. Burant, S. S. Iyengar, J. Tomasi, M. Cossi, N. Rega, J. M. Millam, M. Klene, J. E. Knox, J. B. Cross, V. Bakken, C. Adamo, J. Jaramillo, R. Gomperts, R. E. Stratmann, O. Yazyev, A. J. Austin, R. Cammi, C. Pomelli, J. W. Ochterski, R. L. Martin, K. Morokuma, V. G. Zakrzewski, G. A. Voth, P. Salvador, J. J. Dannenberg, S. Dapprich, A. D. Daniels, O. Farkas, J. B. Foresman,



- J. V. Ortiz, J. Cioslowski and D. J. Fox, *Gaussian 09*, Gaussian, Inc., Wallingford CT, 2013.
- 26 T. Yanai, D. P. Tew and N. C. Handy, *Chem. Phys. Lett.*, 2004, **393**, 51.
- 27 D. M. P. Mingos, Structure and Bonding, in *Gold Clusters, Colloids, and Nanoparticles II*, ed. D. M. P. Mingos, Springer International Publishing, Berlin, 2014, vol. 162, p. 1.
- 28 X.-Y. Chang, K.-H. Low, J.-Y. Wang, J.-S. Huang and C.-M. Che, *Angew. Chem., Int. Ed.*, 2016, **55**, 10312.
- 29 E. G. Mednikov and L. F. Dahl, *J. Cluster Sci.*, 2005, **16**, 287.
- 30 E. G. Mednikov, N. T. Tran, N. L. Aschbrenner and L. F. Dahl, *J. Cluster Sci.*, 2007, **18**, 253.
- 31 L. C. McKenzie, T. O. Zaikova and J. E. Hutchison, *J. Am. Chem. Soc.*, 2014, **136**, 13426.
- 32 (a) A. Das, C. Liu, H. Byun, K. Nobusada, S. Zhao, N. Rosi and R. Jin, *Angew. Chem., Int. Ed.*, 2015, **54**, 3140; (b) Y. Song, S. Jin, X. Kang, J. Xiang, H. Deng, H. Yu and M. Zhu, *Chem. Mater.*, 2016, **28**, 2609; (c) Y. Wang, H. Su, C. Xu, G. Li, L. Gell, S. Lin, Z. Tang, H. Häkkinen and N. Zheng, *J. Am. Chem. Soc.*, 2015, **137**, 4324; (d) Y. Pei, J. Tang, X. Tang, Y. Huang and X. Zeng, *J. Phys. Chem. Lett.*, 2015, **6**, 1390; (e) L. G. AbdulHalim, M. S. Bootharaju, Q. Tang, S. Gobbo, R. G. AbdulHalim, M. Eddaoudi, D.-e. Jiang and O. M. Bakr, *J. Am. Chem. Soc.*, 2015, **137**, 11970.
- 33 Z. Wang, R. Senanayake, C. M. Aikens, W.-M. Chen, C.-H. Tunga and D. Sun, *Nanoscale*, 2016, **8**, 18905.
- 34 S. Chen, S. Wang, J. Zhong, Y. Song, J. Zhang, H. Sheng, Y. Pei and M. Zhu, *Angew. Chem., Int. Ed.*, 2015, **54**, 3145.
- 35 Z. Luo and A. W. Castleman, *Acc. Chem. Res.*, 2014, **47**, 2931.
- 36 A. Tlahuice-Flores, R. L. Whetten and M. Jose-Yacamán, *J. Phys. Chem. C*, 2013, **117**, 20867.
- 37 F. Sheong, J.-X. Zhang and Z. Lin, *Inorg. Chem.*, 2016, **55**, 11348.
- 38 D. Mingos and Z. Lin, *Comments Inorg. Chem.*, 1989, **9**, 95.
- 39 (a) Y. Niihori, M. Eguro, A. Kato, S. Sharma, B. Kumar, W. Kurashige, K. Nobusada and Y. Negishi, *J. Phys. Chem. C*, 2016, **120**, 14301; (b) Y. Negishi, W. Kurashige, Y. Niihori, T. Iwasab and K. Nobusada, *Phys. Chem. Chem. Phys.*, 2016, **18**, 1397; (c) B. Molinää and A. T. Flores, *Phys. Chem. Chem. Phys.*, 2009, **11**, 7123.
- 40 K. Kwak, Q. Tang, M. Kim, D.-e. Jiang and D. Lee, *J. Am. Chem. Soc.*, 2015, **137**, 10833.

